WILEY | Hindawi

Research Article

Hot-Antisolvent Assisted Morphological Regulation of Perovskites for Semitransparent Photovoltaics Employing Hot-Pressing Approach

Dong-Gun Lee,[1] Padmini Pandey,[1] Jitendra Bahadur,[2] Jun Tae Song,[3,4] Jung Sang Cho [ID],[5] and Dong-Won Kang [ID] [1,2]

[1]Department of Smart Cities, Chung-Ang University, Seoul 06974, Republic of Korea
[2]Department of Energy Systems Engineering, Chung-Ang University, Seoul 06974, Republic of Korea
[3]Department of Applied Chemistry, Faculty of Engineering, Kyushu University, Motooka 744, Nishi-ku, Fukuoka 819-0395, Japan
[4]International Institute for Carbon-Neutral Energy Research (WPI-I2CNER), Kyushu University, Motooka 744, Nishi-ku, Fukuoka 819-0395, Japan
[5]Department of Engineering Chemistry, Chungbuk National University, Cheongju, Chungbuk 361-763, Republic of Korea

Correspondence should be addressed to Jung Sang Cho; jscho@cbnu.ac.kr and Dong-Won Kang; kangdwn@cau.ac.kr

The processing of halide perovskites in the air significantly influences their morphology and surface coverage, often leading to the presence of numerous trap densities that adversely affect device performance. In this study, we explored the development of perovskite films using a solvent extraction method, where the temperature of the anisole antisolvent was varied. Our findings demonstrate that the hot-antisolvent strategy effectively controls nucleation, resulting in the formation of highly dense, pinhole-free, and crack-free perovskite films with reduced surface roughness. Films fabricated using this hot-antisolvent approach exhibited enhanced photoluminescence, indicating lower trap density and increased recombination resistance. They also showed slower charge carrier recombination rates and efficient charge extraction, suggesting the suppression of nonradiative recombination. Furthermore, the superior quality of perovskite films obtained through the hot-antisolvent strategy significantly enhanced the power conversion efficiency (PCE) of hot-pressed semitransparent perovskite solar cells. The PCE remarkably increased from 0.13% to an impressive 12.65% while maintaining an average visible transmittance of 26.55% and exceptional air stability for 2000 hours with no significant degradation in initial PCE. This study achieves a record-breaking light utilization efficiency of 3.36% in the realm of research on hot-press processes.

1. Introduction

Organic-inorganic halide perovskite materials have been extensively investigated as efficient solar absorbers in perovskite solar cells (PSCs) for more than a decade [1–6]. The outstanding defect tolerance and electronic properties of halide perovskites (HPs) such as low exciton binding energy (20 meV), strong absorption coefficient (10^5 cm^{-1}), superior carrier lifetime, long carrier diffusion length (>1 micron), and high carrier mobility [7–10] make them highly desirable in PSCs which successfully reached from 3% to 25.8% of power conversion efficiency (PCE) till date [11]. Several approaches have been implemented to regulate the crystallization of perovskite films with improved morphology such as solution processing [12, 13], precursor engineering [14], additive assisted method [15–17], and hot-air blow method [18–20]. Among several strategies, solvent extraction (solution processing) is a highly effective and broadly used technique to achieve dense and highly crystalline perovskite film [12, 13].

In the solution processing techniques, the formation of perovskite film is a two-step process, i.e., nucleation and crystal growth. The formation of nuclei is typically influenced by the Gibbs free energy disparity among the

interfacial energies of the surface and bulk of the system. Antisolvent treatment enables the perovskite solution to achieve a supersaturation state, which is a prerequisite for the nucleation process to initiate [21, 22]. The most common antisolvents used in solvent extraction methods are chlorobenzene, toluene, and diethyl ether [23–25]. The fabrication of high-quality perovskite film depends upon controlled nucleation and crystal growth. Taherianfard et al. investigated that the commonly used antisolvent (chlorobenzene) temperature can control the nucleation to crystallization of perovskite which is $(FAPbI_3)_{0.85}(MAPbBr_3)_{0.15}$ with a bandgap of 1.56 eV, reached to device efficiency of 20% [26]. In another report by Ren et al., antisolvent temperature-assisted nucleation to growth phenomenon was discussed, according to which cold antisolvent treatment (inert processing conditions) led to develop high efficiency (19.2%) PSCs using $MAPbI_3$ with bandgap of 1.53 eV as a perovskite layer [27], although such high device performance through solvent extraction approach is reached by using halogenated antisolvents under inert processing conditions. Instead, an ecofriendly antisolvent such as anisole with a comparatively higher boiling point (154°C) and low toxicity is an alternative to halogenated antisolvents. Yavari et al. studied anisole antisolvent in the solvent extraction process and demonstrated high PCEs of 19.9% (inside the glove box) and 15.5% (in ambient air conditions) [28]. PSCs could be made with excellent performance under inert processing conditions, on the other hand, the requirements of controlled processing in inert conditions greatly increase the production cost which limits the commercialization. While in ambient air processing conditions, it is challenging to control the nucleation to crystal growth due to the sensitivity of HPs towards oxygen, humidity, etc. [29, 30]. Regarding the impact of humidity on perovskite film growth, Gao et al. have shown that a low nucleation density, resulting from decreased supersaturation under high humid conditions, leads to the island-like growth of perovskite films. Conversely, a high nucleation density is observed under low humid conditions [31]. With respect to oxygen, Cheng et al. discovered that its presence alters the surface energy of interlayer materials. This alteration causes the dewetting of PbI_2 solution on substrates, particularly on hydrophobic organic materials [32]. These factors can therefore pose significant challenges in producing high-quality perovskite films and achieving consistent reproducibility.

In the present work, we fabricated pinhole-free and highly dense perovskite film (1.65 eV) with surface uniformity under ambient air processing by using a heated antisolvent (anisole) strategy and postannealing. A systematic analysis was conducted with a wide range of heated antisolvent (0 to 100°C) treatments in solution processing followed by a subsequent annealing step. The investigation revealed that heated antisolvent treatment strongly improved the quality of perovskite film by controlling nucleation to intermediate phase formation and delivered proper crystal growth with desirable uniformity and reduced pinholes. The champion device reached a respectably high efficiency of 16.72% when perovskite film was treated with anisole (75°C) during solvent extraction, while with room tempera-

ture (RT) anisole (25°C), the PSC delivered 15.53% efficiency. Furthermore, we extended our study to fabricate semitransparent PSCs with hot pressing method to demonstrate the utility of our proposed heated antisolvent approach. Based on the observations, a plausible mechanism is suggested by affirming that the nucleation stage governs the intermediate phase morphology. Hence, the suitable elevation of antisolvent temperature performed in this work benefits to regulate the nucleation to intermediate phase formation and further crystal growth, which leads to developing dense, pinhole-free perovskite film. Furthermore, we chose two films, namely, A-25°C and A-75°C to fabricate the PSC device through the hot press method on a transparent substrate, and the results obtained were interesting because the A-25°C device showed almost 0% PCE due to the rough surface and the existence of several cracks in the perovskite film, whereas A-75°C device acquired respectable high efficiency of 12.65% through hot pressing method of PSC with average visible transmittance (AVT) of 26.55%. Light utilization efficiency (LUE), calculated by multiplying PCE by AVT values, is a useful criterion for assessing the performance of semitransparent solar cells. We have achieved a remarkable LUE of 3.36% which represents the highest LUE among the hot-pressed semitransparent PSCs studied for both PCE and AVT. Additionally, we observed excellent device stability in the A-75°C hot press condition, with negligible PCE loss in ambient air over a period of 2000 h.

2. Experimental Methods

2.1. Materials. Indium tin oxide (ITO) coated glasses ($10\,\Omega$ sq^{-1}, AMG) were used as substrates for perovskite solar cells. For cleaning the substrates, acetone (99%, SAMCHUN) and isopropyl alcohol (IPA, 99.5%, SAMCHUN) were used. n-Butylammonium iodide (n-BAI, 99%, GreatCell Solar), lead iodide (PbI_2, 99.99%, Tokyo Chemical Industry), lead bromide ($PbBr_2$, 99.999%, Alfa Aesar), formamidinium iodide (FAI, 99%, GreatCell Solar), and cesium bromide (CsBr, 99.999%, Alfa Aesar) were used as the perovskite precursors. For the perovskite precursor solvents, dimethyl sulfoxide (DMSO, 99.8%, SAMCHUN) and dimethylformamide (DMF, 99.5%, SAMCHUN) were used. Anisole (99%, Alfa Aesar) was utilized for antisolvent treatment in this study.

2.2. Device Fabrication. ITO glasses were cleaned sequentially with acetone and IPA by the ultrasonic cleaner for 20 min each. After that, the ITO glasses were dried in the oven for 20 min to evaporate cleaning solvents. UV-ozone treatment was conducted on the dried ITO substrates for 30 min to enhance the wettability and eliminate residual contaminants on the surface. To form the hole transport layer (HTL), NiO_X precursor which was prepared by mixing 0.233 g of nickel nitrate hexahydrate in 1 mL of ethylene glycol and $53.6\,\mu L$ of ethylenediamine was spin-coated onto the ITO substrates at 5000 rpm for 50 s, then they annealed at 300°C for 1 h in air. 0.4 mg/mL solution of [2-(3,6-dimethoxy-9H-carbazol-9-yl)ethyl]phosphonic acid (MeO-2PACz, 98.0%, Tokyo Chemical Industry) in ethanol

was spin-coated onto the NiO_X coated substrates at 5000 rpm for 20 s and annealed at 100°C for 10 min. $BA_{0.02}(FA_{0.83}Cs_{0.17})_{0.98}Pb(I_{0.83}Br_{0.17})_3$ perovskite was used in this study as an absorber layer (details of perovskite solution preparation are described in our previous study). [33] 70 μL of the perovskite precursor was spin-coated at 4000 rpm for 30 s on the HTL, during the spin-coating, 0.5 mL of anisole (with different temperatures from 0°C to 100°C) was dripped at 25th second onto the substrate and annealed at 120°C for 10 min on a hot plate in ambient air. To form the electron transport layer (ETL), a 20 mg/mL solution of phenyl-C61-butyric acid methyl ester ($PC_{61}BM$, 99.5%, Organic Semiconductor Materials) in chlorobenzene and dichlorobenzene mixture (3 : 1) was spin-coated onto the perovskite film at 1500 rpm for 25 s and annealed at 110°C for 5 min. Bathocuproine (BCP, 0.5 mg/mL in isopropanol) was spin-coated subsequently onto the $PC_{61}BM$ layer at 4000 rpm for 20 s. Finally, silver (Ag) electrodes were thermal-evaporated on the ETL under high vacuum ($<1 \times 10 - 6$ Torr). A schematic illustration of the device fabrication process is given in Figure S1.

2.3. Hot Pressed Device Fabrication. Fabrication of the lower substrate which was stacked as glass/ITO/NiO_X/MeO-2PACz/perovskite is the same as fabrication of the conventional device up to the perovskite layer deposition. The upper substrate was stacked as glass/ITO/SnO_2. ITO substrates (2 cm × 2 cm) were cleaned and further treated with UV-ozone plasma for 20 min. To form the electron transport layer (ETL), tin oxide colloidal solution (15% in H_2O, Alfa Aesar) was further diluted in deionized water with 1 : 2 ratio. The solution was spin-coated onto the ITO surface at 3000 rpm for 30 s, followed by subsequent annealing at 180°C for 30 min. As made, lower and upper substrates were pressed by using a hot press machine (QM900S, QMESYS Inc.) at 1 MPa, then, the plates' temperature increased to 120°C. When the temperature reached 120°C, pressing pressure increased to 10 MPa, the heater was turned off, and the plates were cooled down to 60°C. After cooling, the pressure was released to 0 MPa. Schematic illustrations of the device fabrication process prepared by the hot press method as well as the hot-pressed device architecture are provided in Figure S2.

2.4. Characterization. Top views and cross-sectional images of the perovskite film were observed by field emission scanning electron microscopy (FE-SEM; SIGMA 300, Carl Zeiss) at different magnifications. Perovskite crystallinity and phase purity were detected by Bruker-AXS (New D8-Advance, Bruker) using Cu Kα radiation with a scan rate of 11° min^{-1}. Atomic force microscopy (AFM) (Park Systems, NX-10) was used with noncontact mode to observe the surface topography of perovskite film. The absorbance spectra of the films and transmittance spectrum of the hot-pressed device were measured by ultraviolet-visible (UV–Vis) spectroscopy (UV-2700, Shimadzu). All device characterizations were carried out in ambient conditions (RT and RH of 20~30%). Steady-state photoluminescence (SS-PL) measurement of the films was conducted using a spectroflu-

orometer (FP-8600, Jasco). J-V curves of the PSCs and light intensity dependence of J_{sc} and V_{oc} were measured using a solar simulator (PEC-L01, Peccell Technologies). J-V curves were obtained under standard AM 1.5 G illumination (power, 100 mW cm^{-2}), and hot-pressed device J-V characteristic graphs were measured under a photomask of 4 mm^2 active cell area definition. The EQE measurement was performed using a power source (Abet Technologies 150 W Xenon lamp, 13014) with a monochromator (DongWoo Optron, MonoRa500i) and a CompactStat (Ivium Technologies; Eindhoven, The Netherlands) to detect responses as a function of the spectral wavelengths. Electrochemical impedance spectroscopy (EIS) was measured using the same equipment with an applied voltage of 0.7 V and a frequency range of 1 MHz–10 Hz. Dark J-V characteristic was measured by Keithley 2400 source meter with a voltage range of 0 V–3 V in a dark condition. Transient photovoltage (TPV) and transient photocurrent (TPC) measurements were carried out with an organic semiconductor parameter system (T400, McScience) comprising a Tektronix oscilloscope (DPO-2014B) 100 MHz bandwidth. Carrier lifetime and extraction time were calculated through biexponentially fitting.

3. Results and Discussion

To systematically investigate the effect of antisolvent temperature on the formation of perovskite film, we utilize anisole as antisolvent with different temperatures dripped onto the spin-coated perovskite film at 25th sec. during the spinning process before final annealing at 120°C. The perovskite films here are coded as A-0°C, A-25°C, A-50°C, A-75°C, and A-100°C, where A stands for anisole-treated sample and 0-100°C stands for different temperatures of the anisole antisolvent as detailed information is provided in the experimental section. Figure 1 shows the FE-SEM top view and cross-sectional images of grown perovskite films before thermal postannealing where anisole antisolvent at different temperatures, i.e., cold (A-0°C), room temperature (A-25°C), and hot (A-50°C, A-75°C, and A-100°C) dripped onto the perovskite during the solvent extraction step. A clear reflection of nonuniform surface was observed with several pinholes (Figure 1(a)) (A-0°C). It is manifested that cold antisolvent (A-0°C) dripping may not be appropriate for extracting DMF/DMSO and the melting point of DMSO in precursor solution is nearly 19°C, which may lead to the trapping of DMSO below its melting point, and the remaining solvent forms pinholes after final annealing step [26]. Multiple grains with pinholes were observed for A-25°C, as shown in Figure 1; however, the nucleation to intermediate phase formation with comparatively improved surface coverage was noticed for A-50°C. We further monitored perovskite intermediate film for A-75°C, where the FE-SEM top view and cross-sectional images (Figure 1) exhibit much dense, intermediate film with better surface uniformity and maximum coverage without pinholes. We may assume that the cold and RT antisolvent treatments are not appropriate to achieve the supersaturation state during spinning, which eventually leads to random distribution in A-0°C and A-
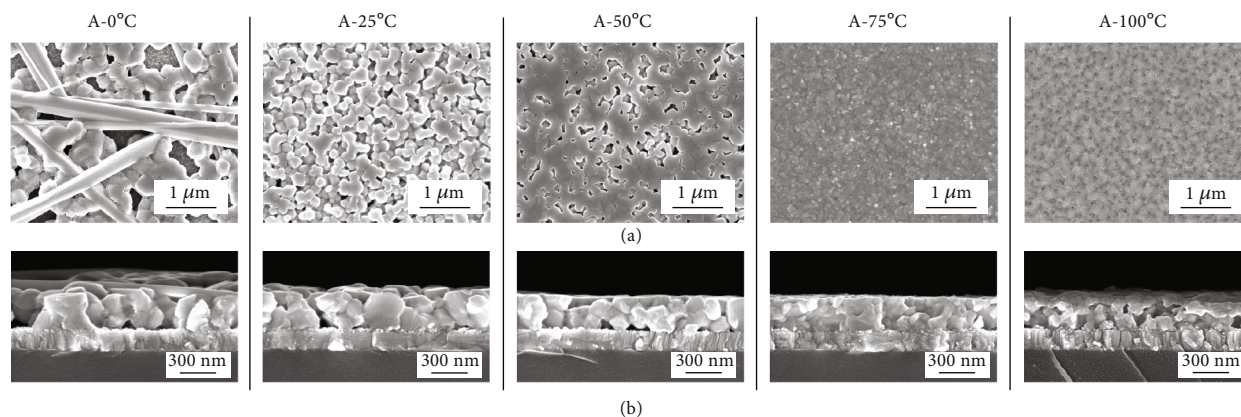
| A-0°C | A-25°C | A-50°C | A-75°C | A-100°C |

(a)

(b)

Figure 1: FE-SEM (a) top view images and (b) cross-sectional images of perovskite films before final annealing at 120°C, where A-0°C, A-25°C, A-50°C, A-75°C, and A-100°C stand for perovskite films treated at different antisolvent temperatures, respectively.

25°C (Figure 1(a)) intermediate perovskite film with low coverage and pinholes. As shown in Figure 1(a) for A-50°C to A-75°C, the intermediate perovskite phase became highly dense with surface uniformity. It is further demonstrated that the elevation of antisolvent temperature to 75°C facilitates fast solvent evaporation that leads to uniform dispersal of perovskite nuclei and dense intermediate phase forms. However, with further increasing antisolvent temperature to 100°C (A-100°C), the perovskite intermediate film quality became poor, as demonstrated through the FE-SEM image, and clear pinholes were detected in the cross-sectional image, which might be due to the faster evaporation of polar solvent from the surface.

Furthermore, the morphology and crystallinity information of postannealed perovskite films were collected from FE-SEM (top images and cross-sectional view) and XRD data, as shown in Figure 2 and Figure S3, respectively. The XRD patterns of perovskite films postannealing (Figure S3) with diffraction peaks at 14.17°, 20.0°, 24.6°, 28.53°, 31.92°, and 35.4° attribute to (100), (110), (111), (200), (210), and (220) hkl planes of α-phase perovskite, as reported in literature [34]. No other impurity peak was observed in the XRD patterns, indicating the formation of pure α-phase perovskite films. The top view FE-SEM micrograph (Figure 2(a)) as depicted for A-0°C and A-25°C annealed films shows several pinholes. At the postannealing stage, the removal of residual polar solvent (DMSO) led to volume contraction and formed several pinholes in A-0°C. The surface inhomogeneity of the intermediate phase (A-0°C and A-25°C (Figure 1(b)) before annealing was clearly reflected in the final film even after postannealing at 120°C. Also, the cross-sectional view of A-0°C and A-25°C films revealed nonuniformity in the formation of final perovskite films (Figure 2(b)). The denseness increased without pinholes in A-50°C postannealed perovskite film (Figures 2(a) and 2(b)); however, slight surface inhomogeneity was observed. The postannealed film from A-75°C shown in Figure 2(a) top view and Figure 2(b) cross-sectional image is significantly dense and uniform without pinholes. Moreover, A-100°C postannealed perovskite film exhibits poor film morphology with nonuniformity and pinhole, as

shown in Figures 2(a) and 2(b). In addition, Figure 2(c) depicts the images of postannealed perovskite films for further visualization. Poor surface image was observed for A-0°C as explained above. In the case of A-25°C perovskite film, several cracks were realized which were slightly reduced for A-50°C, notably, almost no cracks were monitored for A-75°C perovskite film. We have demonstrated the same trend through FE-SEM, as shown in Figure S4, in that the A-25°C showed several cracks with large pinholes. We may expect that the supersaturation state was not reached for nucleation during the set processing time range. This led to the random distribution of nuclei and the formation of a nondense intermediate film with pinholes. The cause of crack generation is known as the compressive capillary force exerted between perovskite grains by the liquid menisci formed at the top surface of the grains during solvent evaporation (extraction) [35]. However, in the case of A-75°C, controlled nucleation occurs as the supersaturation state is reached within the specified processing time. This leads to the formation of dense nuclei and an intermediate film, leaving no gaps for the capillary force to act between the perovskite grains; ultimately, the intermediate film turned to be highly dense, resulting in crack/pinhole-free and uniform perovskite film after the annealing. Hence, the surface morphology determination revealed that 75°C temperature of ecofriendly anisole antisolvent (A-75°C) during the solvent extraction step is the optimal temperature to achieve highly dense perovskite film with controlled morphology, improved film quality, and surface uniformity.

As per the observations from FE-SEM micrographs (Figure 2), the surface topography analysis of selected perovskite films, namely, A-25°C and A-75°C was further conducted using AFM (each perovskite film fabricated on a hole transport layer) to investigate the surface roughness and uniformity. Figures 3(a)–3(d) depict the 2D and 3D AFM micrographs for A-25°C and A-75°C perovskite films at a scale of $4\,\mu m \times 4\,\mu m$. The surface roughness R_a (averaged value) of approx. 16.1 nm was observed for A-25°C postannealed perovskite film. We speculate that anisole dripping at RT to reach the supersaturation stage for the initiation of nucleation may not be the suitable temperature to
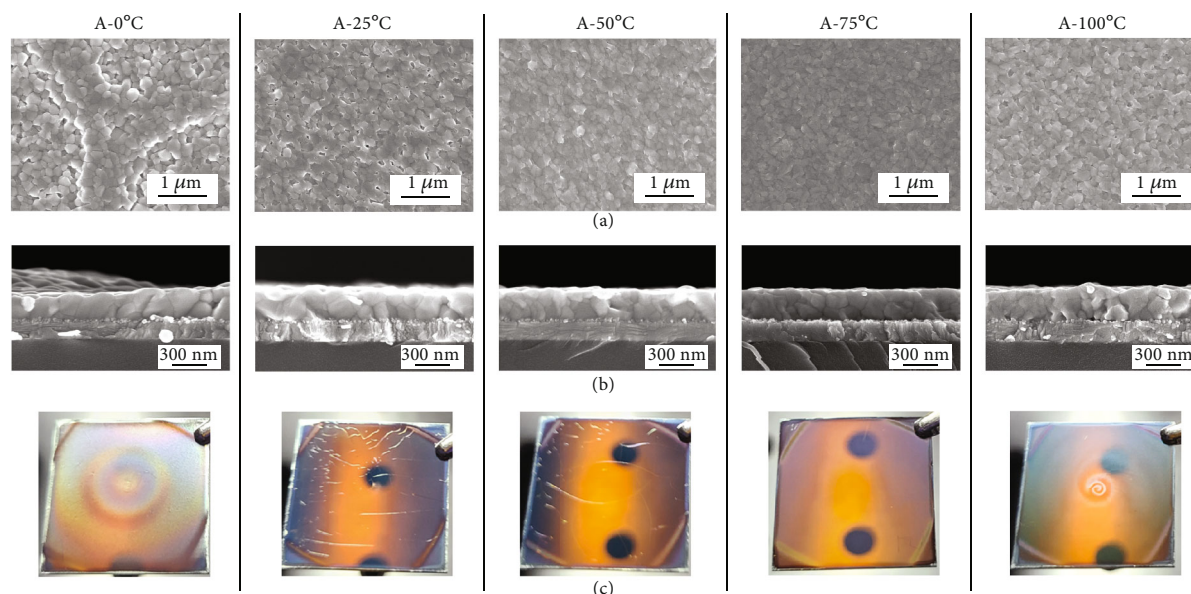
FIGURE 2: FE-SEM (a) top view images and (b) cross-sectional images of perovskite films postannealed at 120°C. (c) Photographic visualization of postannealed perovskite films.

control the perovskite crystal growth, eventually leading to surface nonuniformity, as also depicted in the FE-SEM cross-sectional image. On the other hand, the R_a value for A-75°C film reduced to 10.0 nm that agrees well with the much dense topography shown in the above FE-SEM (Figure 2). It further affirms that the elevation of antisolvent temperature to an optimal range can initiate the nucleation in a controlled manner; hence, 75°C heated anisole treatment during solvent extraction led to the formation of dense and surface uniform perovskite film. Figure 3(e) represents the UV-visible absorbance spectra of A-25°C and A-75°C perovskite $(BA_{0.02}(FA_{0.83}Cs_{0.17})_{0.98}Pb(I_{0.83}Br_{0.17})_3)$ films with similar band edge for both the films. The bandgap of approximately 1.65 eV, calculated from the Tauc plot (Figure 3(f)), is nearly comparable to the bandgap reported in previous studies [36, 37]. In comparison to the A-25°C postannealed perovskite film, the A-75°C perovskite film (Figure 3(e)) exhibited a slight increase in the absorption signal over the whole absorption range. It is attributed to dense film formation and the absence of pinholes and cracks which can be light penetration paths. Furthermore, the steady-state photoluminescence (SS-PL) spectra (Figure 3(g)) show emission wavelength at 746 nm, where the PL intensity enhancement in A-75°C perovskite film implies suppressed nonradiative recombination, which agrees well with the above morphology analysis. Pinholes and cracks in A-25°C perovskite film are prone to be nonradiative recombination spots due to defects on their surface on them. On the other hand, in the case of A-75°C, the dense and uniform film lessens nonradiative recombination spots.

Based on the above results, we suggest a schematic illustration as depicted in Figure 4 which shows the fabrication of perovskite films through RT (A-25°C) and hot (A-75°C) antisolvent strategy followed by a postannealing step. In the conventional methods, the antisolvent dripping over

perovskite solution leads to accomplishing the supersaturation state to initiate the nucleation to intermediate phase formation. Here at RT antisolvent treatment (A-25°C), the supersaturation state was not attained within the processing window. This led to the random distribution of perovskite nuclei and the formation of an intermediate phase with uncontrolled morphology, which produced nonuniform perovskite film with several pinholes postannealing. In the case of the hot-antisolvent strategy (A-75°C), however, the introduction of elevated antisolvent temperature initiates appropriately controlled nucleation within the specified processing duration. This is achieved through fast solvent extraction, which regulates the crystallization of the perovskite material. As a result, a dense, pinhole/crack-free perovskite film is eventually developed. With the findings in the present study, we could state that the film morphology of perovskite material in air processing conditions can be controlled by keenly regulating the nucleation to the intermediate phase formation step.

To examine the impact of hot-antisolvent strategy on photovoltaic performance, we constructed PSCs with glass/ITO/NiO$_X$/MeO-2PACz/perovskite/PCBM/BCP/Ag architecture, as shown in schematic Figure 5(a). The measured current density-voltage (J-V) curves with different temperatures of antisolvent treatment (A-0°C, A-25°C, A-50°C, A-75°C, and A-100°C) were depicted in Figure 5(b) and Figure S5. The detailed photovoltaic (PV) parameters such as short circuit current density (J_{sc}), open circuit voltage (V_{oc}), fill factor (FF), and power conversion efficiency (PCE) corresponding to fabricated PSCs were listed in Table S1.

The A-0°C device reached 13.51% PCE, whereas conventional PSC (A-25°C) showed J_{sc} ~18.99 mA·cm^{-2}, V_{oc} ~1.05 V, and FF ~78.11% with PCE of 15.53%. For A-50°C, a slight enhancement in PV parameters was observed as J_{sc}
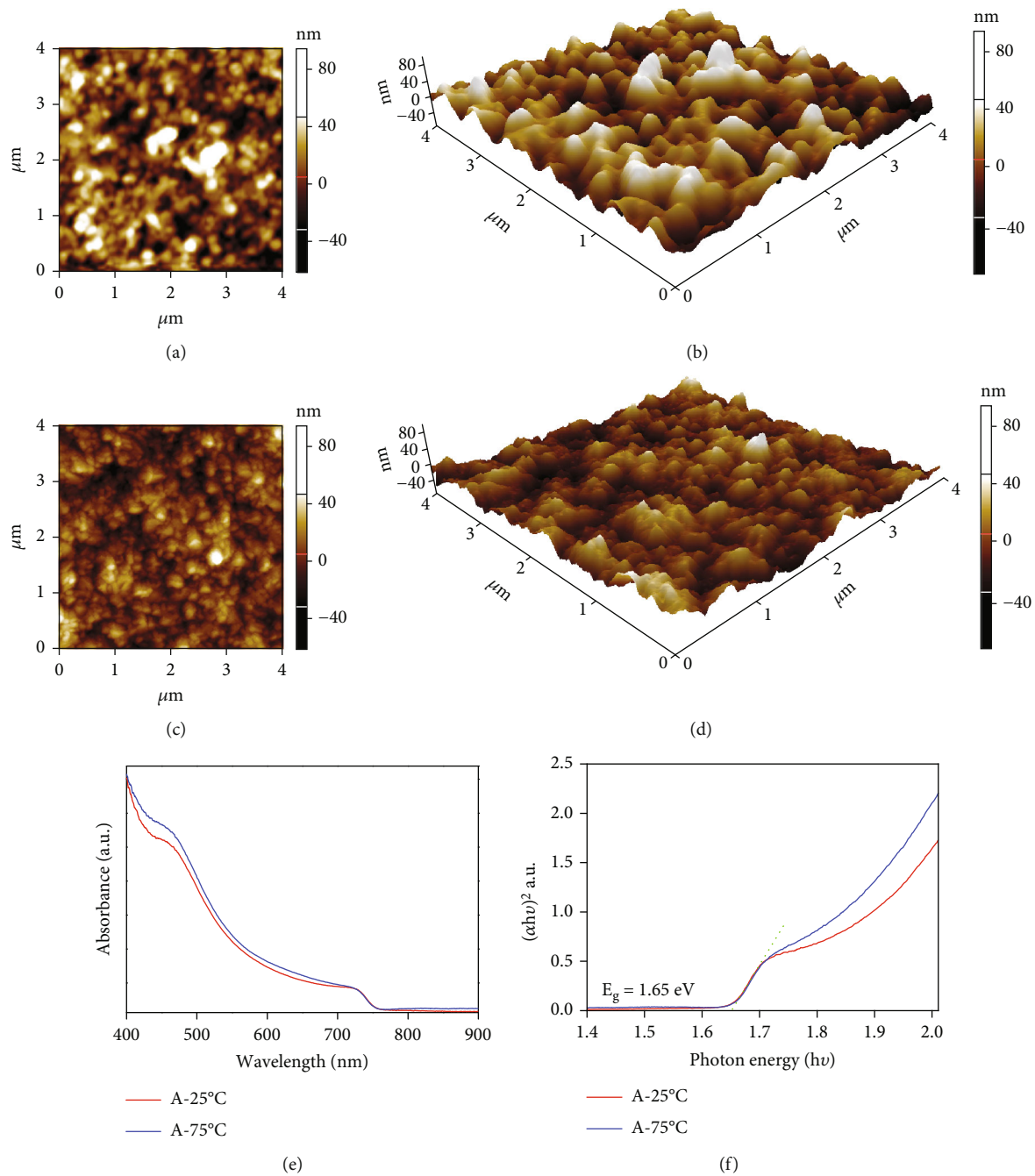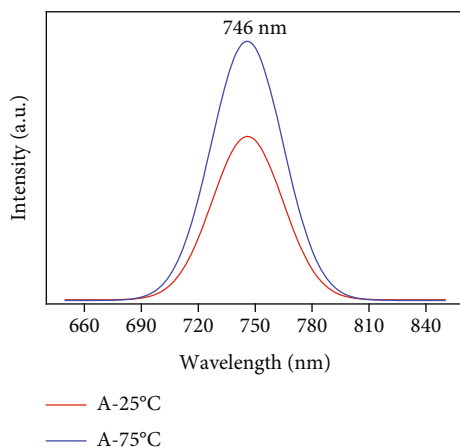
(a)

(b)

(c)

(d)

(e)

(f)

Figure 3: Continued.

(g)

FIGURE 3: (a–d) Atomic force microscopic (AFM) 2D and 3D images of A-25°C and A-75°C with surface roughness. (e) UV-visible absorbance. (f) Tauc plots with bandgap (E_g) of 1.65 eV and (g) PL emission graphs of A-25°C and A-75°C perovskite films postannealed.
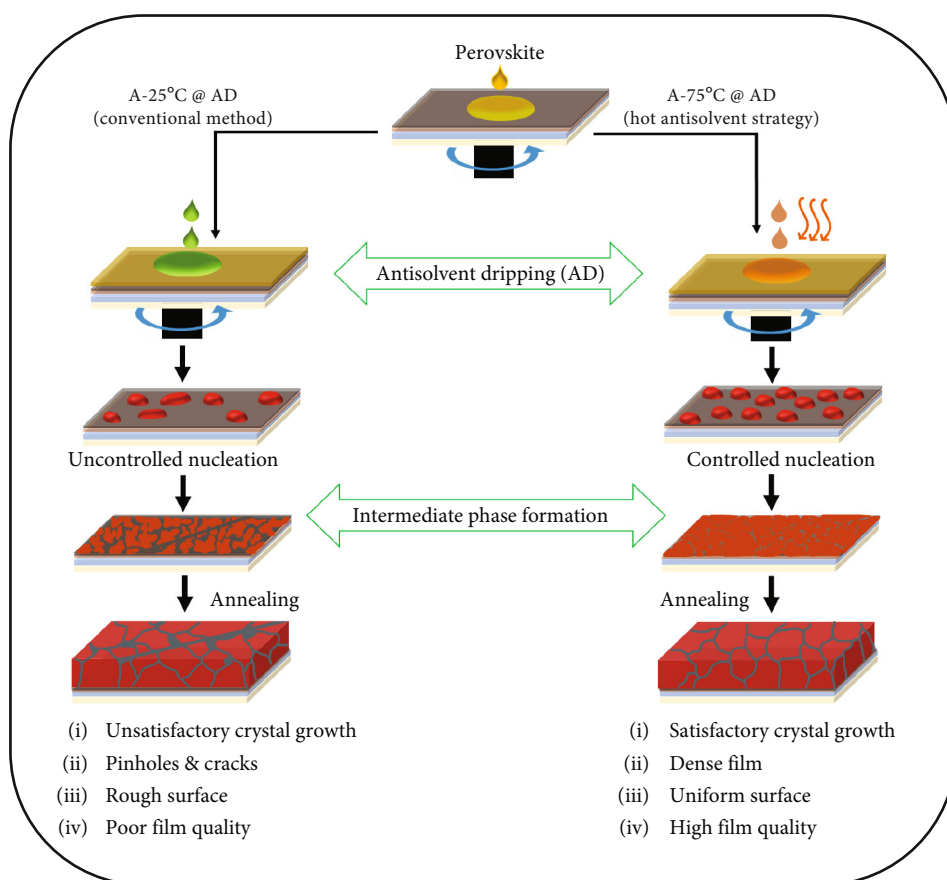

FIGURE 4: Schematic illustration of perovskite film fabrication through a conventional method where the antisolvent temperature is 25°C (A-25°C) and hot-antisolvent strategy (A-75°C).

~19.58 mA·cm^{-2}, V_{oc} ~1.07 V, FF ~78.46%, and PCE of 16.38%. When dripping antisolvent temperature increased to 75°C (A-75°C), PV parameters considerably enhanced as J_{sc} ~19.89 mA·cm^{-2}, V_{oc} of 1.08 V, and FF ~77.61% with champion device PCE of 16.72%. Notably, such significant improvement in PV parameters profited from the suppression of defect-induced recombination due to the formation of dense, uniform, pinhole-free morphology of perovskite film. However, when further antisolvent temperature increased to 100°C (A-100°C), PV parameters reduced as
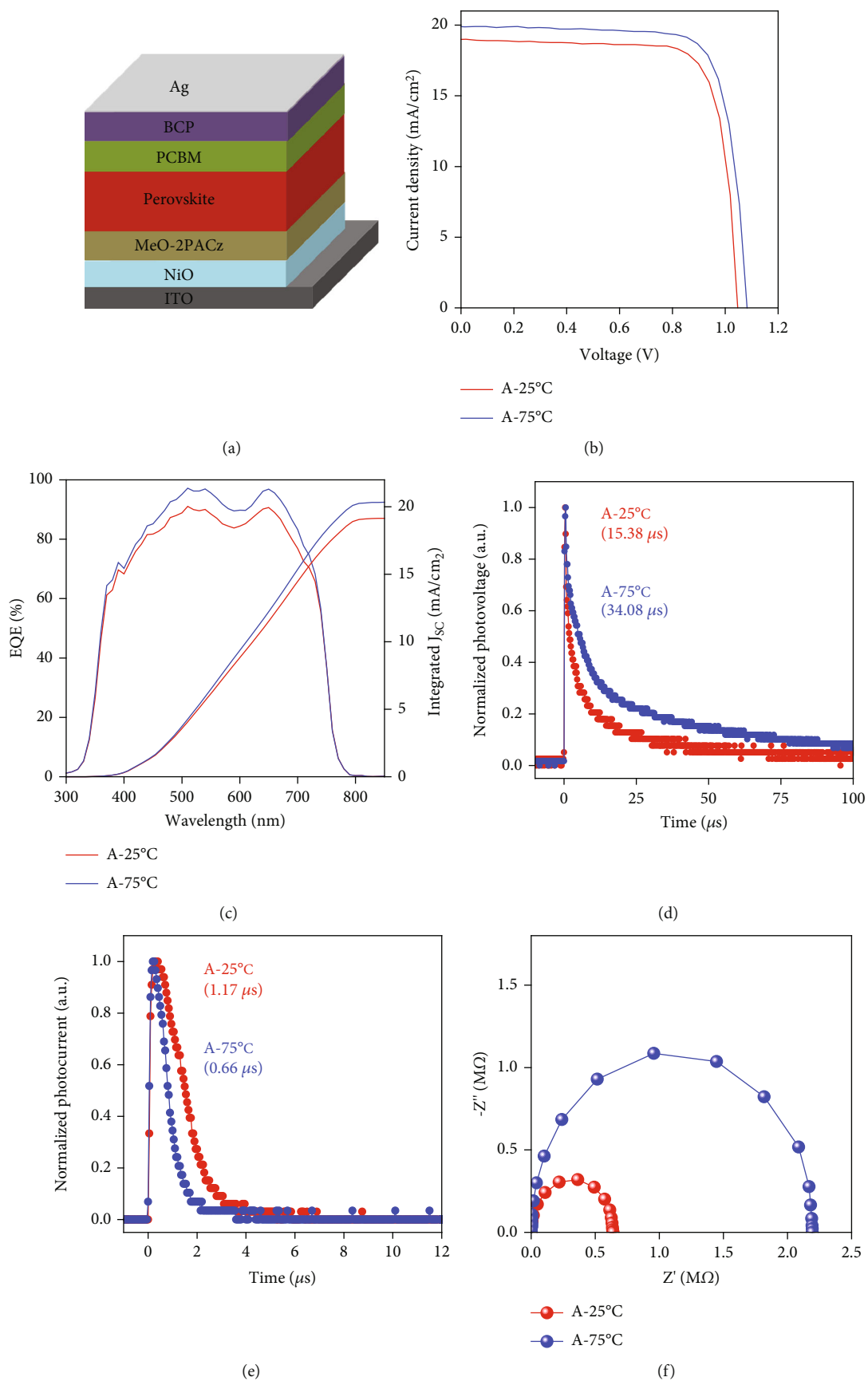
(a)

(b)

(c)
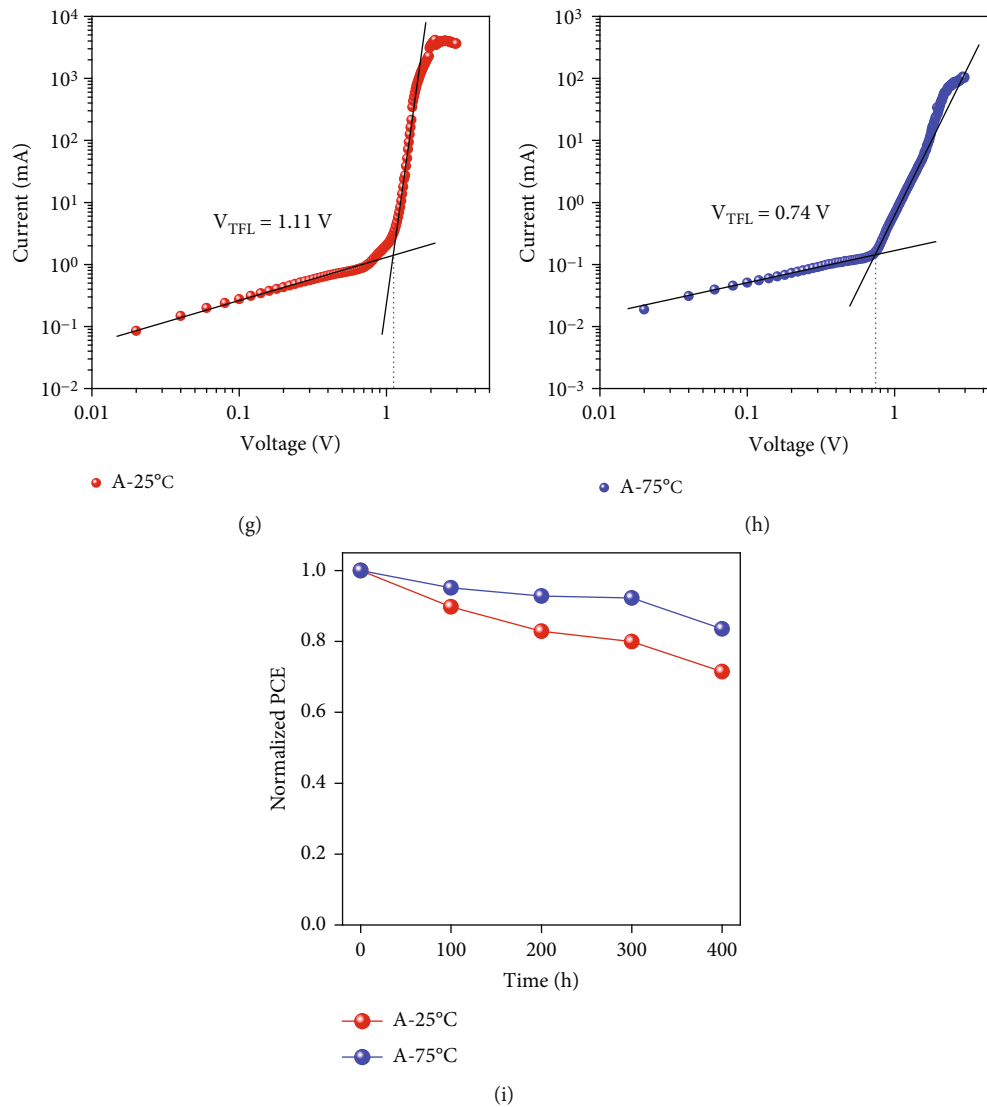
(d)

(e)

(f)

Figure 5: Continued.

(g)

(h)

(i)

FIGURE 5: (a) Schematic illustration of device structure, (b) current density vs. voltage (J-V) graphs, (c) external quantum efficiency and integrated J_{sc} curves, (d) transient photovoltage (TPV), (e) transient photocurrent (TPC), and (f) EIS Nyquist plots for A-25°C and A-75°C, respectively. Defect density analysis through SCLC measurements (g) A-25°C and (h) A-75°C devices. (i) Normalized power conversion efficiency (PCE) graphs for A-25°C (red line) and A-75°C (blue line) PSCs at ambient air conditions.

J_{sc} of 18.51 mA·cm^{-2}, V_{oc} of 1.08 V, FF of 76.89%, and PCE ~15.35% due to degraded surface morphology (Figures 1 and 2) that induced trap-assisted recombination. In addition, the external quantum efficiency (EQE) patterns were recorded corresponding to A-25°C, A-50°C, A-75°C, and A-100°C PSCs, as shown in Figure 5(c) and Figure S6. In comparison to conventional PSC (A-25°C), the optimized device (A-75°C) exhibited higher J_{sc}, which could be also justified by calculating the integrated J_{sc} corresponding to EQE patterns as displayed in Figure 5(c). It is noteworthy that optimized PSC showed higher absorption in a wide range of 350-750 nm than conventional device, suggesting that high-quality perovskite film formed after A-75°C treatment. It has been demonstrated that an improvement in J_{sc} is due to decreased trap-states, increased absorption, better film coverage, and efficient charge transport [27, 38].

To investigate the reproducibility of PSCs, we have fabricated 15 individual PSCs for each case, and the statistical distribution of obtained PV parameters is shown in Figure S7. Interestingly, A-75°C showed a narrow distribution of PV parameters as compared to A-0°C, A-25°C, A-50°C, and A-100°C devices, indicating good reproducibility. Particularly, the A-75°C assisted device exhibited an average PCE of 15.85%, which is higher than that of conventional PSC (A-25°C) and the rest of the cases. Therefore, the nucleation to crystal growth mechanism is much favorable at A-75°C treatment that produces high-quality perovskite film, leading to high PCE with reproducibility in air processing. As indicated above, there have been representative two research works reported for addressing antisolvent temperature effects [26, 27]. They presented perovskite solar cells with decent efficiencies of
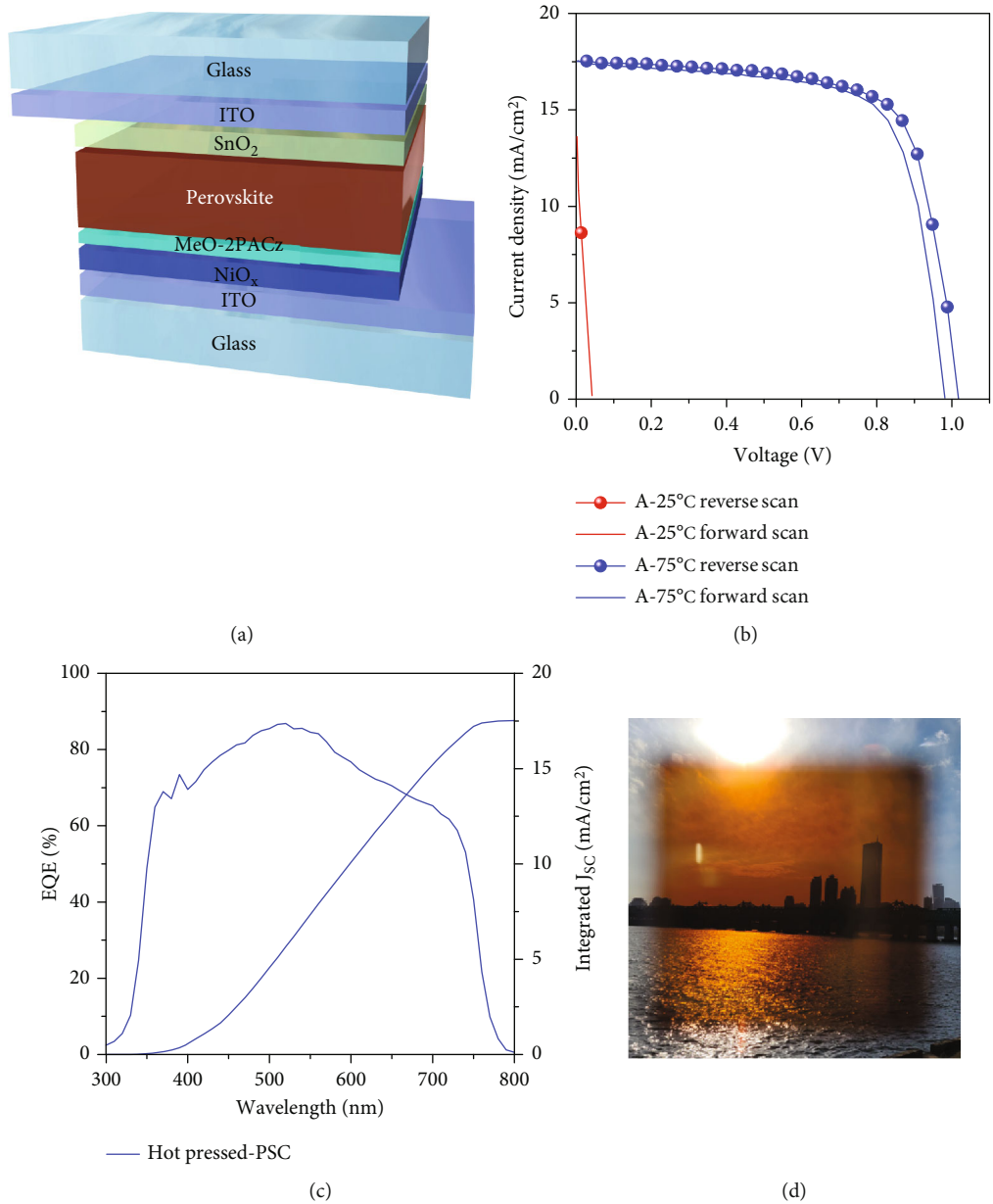
(a)

(b)
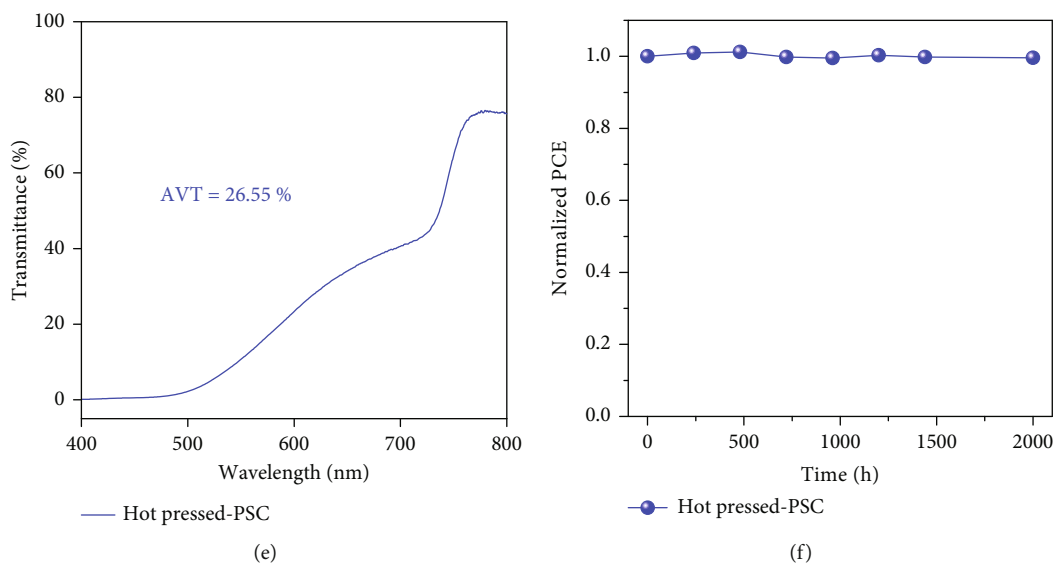

(c)

(d)

Figure 6: Continued.

(e)

(f)

FIGURE 6: (a) Schematic illustration of hot-pressed PSC structure, (b) J-V characteristic curves of A-25°C and A-75°C hot-pressed PSCs in reverse and forward scan, (c) external quantum efficiency curve and integrated J_{sc} curves of A-75°C hot-pressed PSC, (d) photographic visualization of transparent A-75°C hot-pressed PSC, (e) transmittance spectrum and calculated AVT of hot-pressed A-75°C PSC, and (f) 2000 h air stability with normalized PCE of A-75°C hot-pressed device.

19%. However, they used relatively lower bandgap perovskites as light absorber layers which are MAPbI$_3$ (1.53 eV), (FAPbI$_3$)$_{0.85}$(MAPbBr$_3$)$_{0.15}$ (1.56 eV), beneficial for higher overall performance under 1-sun spectrum. On the other hand, we have been using much wider bandgap perovskite BA$_{0.02}$(FA$_{0.83}$Cs$_{0.17}$)$_{0.98}$Pb(I$_{0.83}$Br$_{0.17}$)$_3$ (1.65 eV) than their photoabsorbers to allow for higher optical transmittance because we have been trying to fabricate semitransparent solar cells based on hot-pressing approach. As well-known from the Shockley-Queisser limit, choosing a larger bandgap of a semiconductor could cause lower theoretical efficiency due to reduced optical absorption. Furthermore, perovskite fabrication in our work was done in ambient air condition, while other reported works above fabricated the perovskite films in the N$_2$-filled glove box. Generally, it is hard to form highly crystalline perovskite film in ambient air because of the negative effects of oxygen and moisture [29, 30]. For these reasons, we would like to address here that the efficiencies in our work are relatively moderate compared to other works. However, we targeted semitransparent perovskite cell fabrications under ambient air by employing the hot-pressing approach, which provides a fundamental study on low-cost processing for further commercialization.

In addition, the charge carrier dynamics were further identified through transient photovoltage (TPV) and photo-current (TPC) measurements as shown in Figures 5(d) and 5(e). For conventional (A-25°C) PSC, the calculated charge carrier recombination (τ_{rec}) and transport rate (τ_{ct}) are 15.28 μs and 1.17 μs, while comparatively slow recombination (τ_{rec} ~34.08 μs) with efficient charge extraction (0.66 μs) was realized for the A-75°C PSC champion device. The dense and pinhole-free perovskite film with suppressed

trap states in A-75°C perovskite film is mainly responsible for the improved charge carrier properties. To explore the charge carrier recombination dynamics, we measured the electrochemical impedance spectroscopy (EIS) for A-25°C and A-75°C based PSCs under dark conditions by employing 0.9 V bias voltage and with a frequency range of 1 MHz–100 Hz (Figure 5(f)). The obtained Nyquist plots were fitted according to the equivalent circuit diagram (Figure S8) using Z-view software. The Nyquist plot interception point at the Z' axis (high-frequency region) indicates the value of series resistance (R_s), and the diameter of the semicircle represents the recombination resistance (R_{rec}) value [39]. The value of R_s for A-25°C and A-75°C based devices is 37.8 Ω and 32.4 Ω, respectively, originating from metal wires, metal electrode interface, and ITO electrode interface within the PSCs [40]. Moreover, the R_{rec} value was extracted as 6.44×10^5 Ω and 2.19×10^6 Ω for A-25°C and A-75°C PSCs, respectively. Noticeably, for the A-75°C device, R_{rec} significantly enhanced as compared to the conventional device (A-25°C), which also indicates that nonradiative recombination was remarkably suppressed owing to the formation of pinhole-free, dense, and uniform perovskite film [41].

In order to quantitively evaluate further the defect states, we performed space charge limited current (SCLC) measurement with hole-only device structure (glass/ITO/NiO$_X$/MeO-2PACz/perovskite/P3HT/Ag) under dark conditions and obtained dark current-voltage curves for A-25°C and A-75°C PSCs were shown in Figures 5(g) and 5(h). The value of trap-filled voltage (V_{TFL}) was extracted from the obtained pattern at the kink point, where the current enhanced sharply as depicted in Figures 5(g) and 5(h). The V_{TFL} value was estimated to be 1.11 V and 0.74 V corresponding to A-

25°C and A-75°C based PSCs, respectively. With the help of the V_{TFL} value, we can determine the trap-state density (N_t) using the following equation:

$$N_t = \frac{2\varepsilon_r\varepsilon_o V_{\text{TFL}}}{eL^2},\tag{1}$$

where ε_r, ε_o, e, and L are the dielectric constant, vacuum permittivity, electronic charge, and thickness of perovskite film, respectively [39, 42]. From the above equation, the value of N_t was calculated to be 1.04×10^{16} cm^{-3} and 6.96×10^{15} cm^{-3} related to A-25°C and A-75°C PSCs, respectively. Evidently, A-75°C PSC exhibited reduced defect states as compared to the A-25°C device, suggesting that trap-assisted recombination was effectively suppressed, which is in good agreement with EIS analysis. Device stability was measured under ambient air (~30% RH), as indicated in Figure 5(i). A-75°C PSC maintained 84% of its initial efficiency, while A-25°C maintained 72% of its initial efficiency for 400 h without any encapsulation. The improved stability in A-75°C may be attributed to dense perovskite film formation without cracks or pinholes which can improve resistance against moisture and oxygen penetration.

We fabricated semitransparent PSCs with A-25°C and A-75°C by hot-press lamination process following the structure as shown in Figure 6(a). Hot-pressed devices were fabricated by stacking the lower substrate which consists of glass/ITO/NiO$_X$/MeO-2PACz/perovskite and the upper substrate which consists of glass/ITO/SnO$_2$. They can be combined with each other when proper pressure and heat are applied to them as depicted in Figure S2. J-V characteristics and photovoltaic properties of hot-pressed devices are presented in Figure 6(b) and Table S2. The current density in the J-V curve was calibrated based on integrated J_{sc} obtained from EQE measurement for exact active cell area definition (Figure 6(c)). A-75°C hot-pressed device showed a PCE of 12.65% while the A-25°C hot-pressed device showed a PCE of 0.13% (reverse and forward scans in the case of A-25°C hot-pressed device are completely overlapped because of negligible hysteresis). This huge gap of PCE may be attributed to the vertical shunt through the cracks at the surface of A-25°C perovskite film as shown in Figure 2(c). It was observed that an uncovered large hole in the crack could be a troublesome shunt path contacting HTL with ETL directly at A-25°C perovskite film by FE-SEM image as previously investigated (Figure S4). Meanwhile, there were no observed cracks or uncovered holes at the A-75°C film. Furthermore, a uniform surface of adhesion sides is important to manufacturing high-performance hot-pressed devices. As previously confirmed in FE-SEM and AFM analyses, the surface of A-75°C perovskite film was uniform without pinholes in comparison with the surface of A-25°C film. This dense film formation by hot-antisolvent treatment led to the enhanced photovoltaic performance of the hot-pressed device. We can feasibly observe its impressive transparency by landscape photograph through the device as shown in Figure 6(d). The transmittance spectrum of the A-75°C hot-pressed device is presented in Figure 6(e), and

average visible transmittance (AVT, 400~800 nm) was calculated as 26.55%. The considerable transparency could be easily achieved by applying a rather wide-bandgap perovskite and transparent upper conducting substrates. In addition, hot-pressed PSC was stored in ambient air (~30% RH) and measured to demonstrate the stability of its inherent properties. After the aging test, we found that the device exhibited exceptional reliability by maintaining its initial efficiency with negligible PCE loss for 2000 h (Figure 6(f)) and we are expecting it can maintain the efficiency further longer since then. This outstanding stability is attributed to bilateral transparent substrate covering and protecting perovskite and charge transport layers from humid air and oxygen, etc. Formerly, Jang et al. fabricated hot-pressed semitransparent PSCs with transparent doped graphene anode and cathode and calculated the AVT of the device [43]. They achieved hot-pressed device PCE of 10.73% and AVT of 5%, and detailed information of their result with our result is presented in Table S3. We have achieved a remarkable LUE of 3.36% in this work, whereas previous studies reported an LUE of 0.54%. This is the highest LUE among the hot-pressed semitransparent PSCs studied for both PCE and AVT. Our work implies that controlling the temperature of anisole antisolvent is a critical step to manage the crystalline growth and get optimized perovskite topography with suppressed defects regarding ecofriendly solution processing in ambient air.

4. Conclusion

In summary, we present an effective hot-antisolvent strategy for the fabrication of high-quality perovskite films under ambient air conditions. The antisolvent with different temperatures influences the nucleation to perovskite crystal growth as observed in the present study. Our results suggest that the involvement of optimum temperature (75°C) in antisolvent at the solvent extraction step accelerates the swift nucleation of perovskite by reaching the supersaturation state within the set processing time range. Subsequently created homogeneous nucleation sites ultimately resulted in the formation of a highly dense, pinhole-free, and crack-free perovskite film with a uniform surface under air processing conditions. A significant decrease in trap density states with improved charge carrier extraction rate further confirmed the fabrication of high-quality perovskite film with the proposed strategy. The RT A-25°C champion device showed 15.53% PCE, whereas A-75°C PSC reached to high PCE of 16.72%. We further developed hot-pressed semitransparent PSCs, A-75°C achieved remarkably high device PCE of 12.65%, AVT of 26.55%, a record LUE of 3.36%, and outstanding air stability of 2000 h without degradation. Thus, this strategy is favorable for not only the fabrication and improved quality of perovskite films in an ambient atmosphere but also the hot-press process requiring a highly uniform film surface. This work will contribute to the development of a method for achieving highly uniform perovskite film formation by implementing more precise nucleation control during antisolvent treatment.

Data Availability

The data used to support the findings of this study are available from the corresponding author upon request.

Conflicts of Interest

The authors declare that there is no conflict of interest regarding the publication of this paper.

Authors' Contributions

Dong-Gun Lee and Padmini Pandey contributed equally to this work.

Acknowledgments

Supplementary Materials

Figure S1: schematic illustration of device fabrication process. Figure S2: schematic illustration of device fabrication process prepared by hot press method and hot-press PSC device architecture. Figure S3: X-ray diffraction patterns of perovskite films after annealing at 120°C, where A-0°C, A-25°C, A-50°C, A-75°C, and A-100°C stand for perovskite films treated at different antisolvent temperatures before final annealing, respectively. Figure S4: magnified crack image on A-25°C perovskite film surface and compact A-75°C film without cracks observed by FE-SEM. Figure S5: short circuit current density-voltage (J_{sc}-V_{oc}) characteristic curves of A-0°C, A-50°C, and A-100°C perovskite solar cells, respectively. Figure S6: external quantum efficiency (EQE) curves for A-0°C, A-50°C, and A-100°C perovskite solar cells (PSCs), respectively. Figure S7: device parameters statistical information for A-0°C, A-25°C, A-50°C, A-75°C, and A-100°C PSCs, respectively. Figure S8: equivalent circuit diagram. Table S1: photovoltaic parameters of the various antisolvent temperature treated devices. The values in brackets are averaged over 15 cells. Table S2: photovoltaic parameters hot press device data. Table S3: comparison of semitransparent hot-pressed semitransparent PSCs. (*Supplementary Materials*)

References

[1] J. Y. Kim, J.-W. Lee, H. S. Jung, H. Shin, and N.-G. Park, "High-efficiency perovskite solar cells," *Chemical Reviews*, vol. 120, no. 15, pp. 7867–7918, 2020.

[2] S. Akin, N. Arora, S. M. Zakeeruddin, M. Grätzel, R. H. Friend, and M. I. Dar, "New strategies for defect passivation in high-efficiency perovskite solar cells," *Advanced Energy Materials*, vol. 10, no. 13, article 1903090, 2020.

[3] M. A. Green, A. Ho-Baillie, and H. J. Snaith, "The emergence of perovskite solar cells," *Nature Photonics*, vol. 8, no. 7, pp. 506–514, 2014.

[4] Y. Zhao, H. Xiang, R. Ran, W. Zhou, W. Wang, and Z. Shao, "Beyond two-dimension: One- and zero-dimensional halide perovskites as new-generation passivators for high-performance perovskite solar cells," *Journal of Energy Chemistry*, vol. 83, pp. 189–208, 2023.

[5] S. Shin, P. Nandi, S. Seo, H. S. Jung, N. G. Park, and H. Shin, "Enhancing stability of efficient perovskite solar cells (PCE ≈ 24.5%) by suppressing PbI$_2$ inclusion formation," *Advanced Functional Materials*, vol. 33, no. 40, article 2301213, 2023.

[6] B. Wang, S. Bi, J. Zhou et al., "Enhanced stability in perovskite solar cells *via* room-temperature processing," *Journal of Materials Chemistry C*, vol. 9, no. 41, pp. 14749–14756, 2021.

[7] J. Lim, M. Kober-Czerny, Y.-H. Lin et al., "Long-range charge carrier mobility in metal halide perovskite thin-films and single crystals via transient photo-conductivity," *Nature Communications*, vol. 13, no. 1, p. 4201, 2022.

[8] A. Miyata, A. Mitioglu, P. Plochocka et al., "Direct measurement of the exciton binding energy and effective masses for charge carriers in organic–inorganic tri-halide perovskites," *Nature Physics*, vol. 11, no. 7, pp. 582–587, 2015.

[9] Z. Xiao, Z. Song, and Y. Yan, "From lead halide perovskites to lead-free metal halide perovskites and perovskite derivatives," *Advanced Materials*, vol. 31, no. 47, article 1803792, 2019.

[10] F. Wang, S. Bai, W. Tress, A. Hagfeldt, and F. Gao, "Defects engineering for high-performance perovskite solar cells," *npj Flexible Electronics*, vol. 2, no. 1, p. 22, 2018.

[11] J. Park, J. Kim, H.-S. Yun et al., "Controlled growth of perovskite layers with volatile alkylammonium chlorides," *Nature*, vol. 616, no. 7958, pp. 724–730, 2023.

[12] A. D. Taylor, Q. Sun, K. P. Goetz et al., "A general approach to high-efficiency perovskite solar cells by any antisolvent," *Nature Communications*, vol. 12, no. 1, p. 1878, 2021.

[13] Q. An, L. Vieler, K. P. Goetz et al., "Effect of antisolvent application rate on film formation and photovoltaic performance of methylammonium-free perovskite solar cells," *Advanced Energy and Sustainability Research*, vol. 2, no. 11, article 2100061, 2021.

[14] M. Yang, T. Zhang, P. Schulz et al., "Facile fabrication of large-grain CH$_3$NH$_3$PbI$_{3-x}$Br$_x$ films for high-efficiency solar cells via CH$_3$NH$_3$Br-selective Ostwald ripening," *Nature Communications*, vol. 7, no. 1, article 12305, 2016.

[15] H. Xiao, C. Zuo, L. Zhang et al., "Efficient inorganic perovskite solar cells made by drop-coating in ambient air," *Nano Energy*, vol. 106, p. 108061, 2023.

[16] T. Zhong, K. Tang, W. Xu et al., "NH$_4$Ac boosts the efficiency of carbon-based all- inorganic perovskite solar cells fabricated in the full ambient air to 15.43%," *Applied Surface Science*, vol. 610, p. 155175, 2023.

[17] H. T. Hussein, R. S. Zamel, M. S. Mohamed, and M. K. A. Mohammed, "High-performance fully-ambient air processed perovskite solar cells using solvent additive," *Journal of Physics and Chemistry of Solids*, vol. 149, p. 109792, 2021.

[18] S. S. Mali, J. V. Patil, and C. K. Hong, "Hot-air-assisted fully air-processed barium incorporated cspbi$_2$br perovskite thin films for highly efficient and stable all-inorganic perovskite solar cells," *Nano Letters*, vol. 19, no. 9, pp. 6213–6220, 2019.

[19] J. Su, H. Cai, X. Ye et al., "Efficient perovskite solar cells prepared by hot air blowing to ultrasonic spraying in ambient air," *ACS Applied Materials & Interfaces*, vol. 11, no. 11, pp. 10689–10696, 2019.

[20] Y. Zhou, A. Najar, J. Zhang et al., "Effect of solvent residue in the thin-film fabrication on perovskite solar cell performance," *ACS Applied Materials & Interfaces*, vol. 14, no. 25, pp. 28729–28737, 2022.

[21] S. Song, M. T. Hörantner, K. Choi, H. J. Snaith, and T. Park, "Inducing swift nucleation morphology control for efficient planar perovskite solar cells by hot-air quenching," *Journal of Materials Chemistry A*, vol. 5, no. 8, pp. 3812–3818, 2017.

[22] K. Liao, C. Li, L. Xie et al., "Hot-casting large-grain perovskite film for efficient solar cells: film formation and device performance," *Nano-Micro Letters*, vol. 12, no. 1, pp. 1–22, 2020.

[23] H. Li, Y. Xia, C. Wang et al., "High-efficiency and stable perovskite solar cells prepared using chlorobenzene/acetonitrile antisolvent," *ACS Applied Materials & Interfaces*, vol. 11, no. 38, pp. 34989–34996, 2019.

[24] N. Sakai, S. Pathak, H.-W. Chen et al., "The mechanism of toluene-assisted crystallization of organic–inorganic perovskites for highly efficient solar cells," *Journal of Materials Chemistry A*, vol. 4, no. 12, pp. 4464–4471, 2016.

[25] S.-G. Kim, J.-H. Kim, P. Ramming et al., "How antisolvent miscibility affects perovskite film wrinkling and photovoltaic properties," *Nature Communications*, vol. 12, no. 1, p. 1554, 2021.

[26] H. Taherianfard, G.-W. Kim, M. M. Byranvand et al., "Effective management of nucleation and crystallization processes in perovskite formation via facile control of antisolvent temperature," *ACS Applied Energy Materials*, vol. 3, no. 2, pp. 1506–1514, 2020.

[27] Y.-K. Ren, X.-H. Ding, Y.-H. Wu et al., "Temperature-assisted rapid nucleation: a facile method to optimize the film morphology for perovskite solar cells," *Journal of Materials Chemistry A*, vol. 5, no. 38, pp. 20327–20333, 2017.

[28] M. Yavari, M. Mazloum-Ardakani, S. Gholipour et al., "Greener, nonhalogenated solvent systems for highly efficient perovskite solar cells," *Advanced Energy Materials*, vol. 8, no. 21, article 1800177, 2018.

[29] B. G. Krishna, D. S. Ghosh, and S. Tiwari, "Progress in ambient air-processed perovskite solar cells: insights into processing techniques and stability assessment," *Solar Energy*, vol. 224, pp. 1369–1395, 2021.

[30] I. M. Asuo, D. Gedamu, N. Y. Doumon et al., "Ambient condition-processing strategy for improved air-stability and efficiency in mixed-cation perovskite solar cells," *Materials Advances*, vol. 1, no. 6, pp. 1866–1876, 2020.

[31] H. Gao, C. Bao, F. Li et al., "Nucleation and crystal growth of organic–inorganic lead halide perovskites under different relative humidity," *ACS Applied Materials & Interfaces*, vol. 7, no. 17, pp. 9110–9117, 2015.

[32] Y. Cheng, X. Xu, Y. Xie et al., "18% high-efficiency air-processed perovskite solar cells made in a humid atmosphere of 70% rh," *Solar RRL*, vol. 1, no. 9, article 1700097, 2017.

[33] D.-G. Lee, S. Yoon, H. W. Lee, H. Choi, J. Kim, and D.-W. Kang, "Semitransparent perovskite solar cells with exceptional efficiency and transmittance," *Applied Physics Express*, vol. 14, no. 12, article 126504, 2021.

[34] W. Tan, A. R. Bowring, A. C. Meng, M. D. McGehee, and P. C. McIntyre, "Thermal stability of mixed cation metal halide perovskites in air," *ACS Applied Materials & Interfaces*, vol. 10, no. 6, pp. 5485–5491, 2018.

[35] A. Thote, I. Jeon, J.-W. Lee et al., "Stable and reproducible 2d/3d formamidinium–lead–iodide perovskite solar cells," *ACS Applied Energy Materials*, vol. 2, no. 4, pp. 2486–2493, 2019.

[36] K. A. Bush, A. F. Palmstrom, Z. J. Yu et al., "23.6%-efficient monolithic perovskite/silicon tandem solar cells with improved stability," *Nature Energy*, vol. 2, no. 4, article 17009, 2017.

[37] S. W. Cho, P. Pandey, J. Park, T.-W. Lee, and D.-W. Kang, "Mixed solvent engineering for morphology optimization of the electron transport layer in perovskite photovoltaics," *ACS Applied Energy Materials*, vol. 5, no. 1, pp. 387–396, 2022.

[38] L. Liang, Z. Li, F. Zhou et al., "The humidity-insensitive fabrication of efficient $CsPbI_3$ solar cells in ambient air," *Journal of Materials Chemistry A*, vol. 7, no. 47, pp. 26776–26784, 2019.

[39] S. Fu, J. Wang, X. Liu et al., "Multifunctional liquid additive strategy for highly efficient and stable $cspbi_2br$ all-inorganic perovskite solar cells," *Chemical Engineering Journal*, vol. 422, article 130572, 2021.

[40] A. Guerrero, J. Bisquert, and G. Garcia-Belmonte, "Impedance spectroscopy of metal halide perovskite solar cells from the perspective of equivalent circuits," *Chemical Reviews*, vol. 121, no. 23, pp. 14430–14484, 2021.

[41] J. Bahadur, J. Ryu, P. Pandey, S. Cho, J. S. Cho, and D.-W. Kang, "*In situ* crystal reconstruction strategy-based highly efficient air-processed inorganic $CsPbI_2Br$ perovskite photovoltaics for indoor, outdoor, and switching applications," *Nanoscale*, vol. 15, no. 8, pp. 3850–3863, 2023.

[42] A. B. Niloy, M. Al Razy, S. Ahmed, F. Jannat, and M. A. Alim, "Performance investigation of cesium formamidinium lead mixed halide ($FA_{0.83}Cs_{0.17}PbI_{3-x}Br_x$) for different iodine and bromine ratios," *Micro and Nanostructures*, vol. 168, article 207305, 2022.

[43] C. W. Jang, J. M. Kim, and S.-H. Choi, "Lamination-produced semi-transparent/flexible perovskite solar cells with doped-graphene anode and cathode," *Journal of Alloys and Compounds*, vol. 775, pp. 905–911, 2019.